EES Solar

PAPER

View Article Online
View Journal | View Issue

Cite this: *EES Sol.*, 2025, **1**, 847

Organic solar cells spray-coated in air with enhanced efficiency and stable morphology

Qin Wang,[a] Kang An,*[a] Xin Cui,[a] Xinyu Jiang,*[b] Xingwang Kang,[a] Jingyan Qi,[a] Xujie Hui,[a] Jialin Wu,[a] Xin Zhang,[a] Zhipeng Yin,[a] Wei Meng,[a] Youyu Jiang,*[c] Yinhua Zhou,[c] Keyou Yan,[d] Lei Ying,[a] Stephan V. Roth[be] and Ning Li*[af]

Received 28th May 2025
Accepted 15th August 2025

DOI: 10.1039/d5el00081e

rsc.li/EESSolar

Spray coating is a promising technique for the scalable fabrication of organic solar cells (OSCs) owing to its high compatibility with arbitrarily shaped substrates. However, the insights and analyses from the widely used spin-coating technique cannot be directly transferred to spraying. In this work, we systematically investigate the transformation from conventional spin-coating to spray coating for a representative OSC system, PM6 : DTY6 : L8-BO. The conventionally used chloroform (CF) solvent in spray coating leads to a significant drop in the power conversion efficiency (PCE) and stability, owing to an inferior morphology, while optimized toluene (TL) films enable superior performance and enhanced long-term stability. *In situ* spectroscopy and systematic morphology investigations reveal that the two solvents exhibit distinct film formation kinetics, with TL promoting a more gradual and uniform assembly process, leading to more favorable molecular packing and reduced amorphous clustering. The optimized TL-sprayed device achieved a PCE comparable to the spin-coated one and maintained 97% of its initial performance after 1000 h of thermal aging at 65 °C. These findings highlight the critical role of morphology modification in performance and stability during processing technique transformation.

Broader context

Scaling up the fabrication of organic solar cells (OSCs) is crucial for their commercial application, yet it remains constrained by the limitations of lab-oriented processing methods. Spray-coating, as a scalable and substrate-versatile technique, is attracting increasing attention. However, knowledge derived from conventional spin-coating approaches often proves inadequate when applied directly to spray-coated systems. Simultaneously, the widespread use of halogenated solvents such as chloroform (CF) in high-performance OSCs raises concerns about environmental safety and industrial applicability. The transition from spin-coating to spray-coating introduces markedly different film formation dynamics. The faster solvent evaporation and altered flow behavior during spray-coating lead to different morphology evolution compared to that for spin-coating. In this work, we present a systematic study on process transition from spin-to spray-coating for non-fullerene based OSCs using a non-halogenated solvent system. Our findings demonstrate that toluene enables a more gradual and controlled assembly process during spray deposition, leading to improved morphological order, enhanced device efficiency, and superior morphology stability. This study provides valuable insights into the rational tuning of solvent systems for spray-coated OSCs toward environmentally friendly and scalable manufacturing.

1 Introduction

Great progress has been made in the field of organic solar cells (OSCs) in recent years, due to the continuous development of novel photo-active materials[1–5] and the development of device engineering.[6–10] In particular, the popular non-fullerene acceptors (NFAs) of Y6 and its derivatives have enhanced power conversion efficiencies (PCEs).[11–15] Meanwhile, various optimization strategies for active layers have been utilized to further enable the generation of PCEs of over 20%,[16–21] including the use of liquid/solid additives, multi-component concepts, and active layer structure modification. High-efficiency OSCs are commonly fabricated using spin-coating (SC) on small-area substrates in a nitrogen-filled glove box, and upscaling towards large-scale production is difficult. Developing

[a]*Institute of Polymer Optoelectronic Materials & Devices, Guangdong Basic Research Center of Excellence for Energy and Information Polymer Materials, State Key Laboratory of Luminescent Materials & Devices, South China University of Technology, Guangzhou 510640, China. E-mail: mskangan@scut.edu.cn; ningli2022@scut.edu.cn*

[b]*Deutsches Elektronen-Synchrotron, 22607 Hamburg, Germany. E-mail: xinyu.jiang@desy.de*

[c]*Wuhan National Laboratory for Optoelectronics, Huazhong University of Science and Technology, Wuhan 430074, China. E-mail: youyujiang@hust.edu.cn*

[d]*School of Environment and Energy, State Key Laboratory of Luminescent Materials and Devices, Guangdong Provincial Key Laboratory of Solid Wastes Pollution Control and Recycling, South China University of Technology, Guangzhou, China*

[e]*Department of Fibre and Polymer Technology, KTH Royal Institute of Technology, SE-100 44 Stockholm, 510640, Sweden*

[f]*Guangdong Provincial Key Laboratory of Luminescence from Molecular Aggregates, South China University of Technology, Guangzhou, China*

compatible large-area coating technologies under an ambient atmosphere is essential to produce high-throughput and low carbon footprint organic photovoltaic. Spray coating (SP) is a promising method, as it offers surface compatibility, efficient material utilization, and suitability for continuous production (Fig. 1a). There are reports on spray-coated OSCs fabricated with the addition of four-electrode electrospray that have achieved a PCE approaching 16% by compressing a circular profile into a sheet-like one to eliminate coffee-ring effects.[22] Ultrasonic spray assisted by an air knife can also promote the spread of wet films across the entire surface, resulting in uniform photo-active layers.[23] The optimization of spray-coated photo-active layers has been focused on material design, solvent screening, and post-treatments, leading to continuous improvement for spray-coated OSCs.[24–27]

Ensuring long-term operational stability remains a major obstacle for the commercial viability of OSCs. The gradual transition of the initially optimized bulk heterojunction (BHJ) morphology into an intermediate metastable state, and finally to thermodynamic equilibrium, along with the reorganization of molecular aggregation. or NFA crystallization, and phase separation, leads to unexpected degradation in exciton dissociation, charge carrier transportation and non-radiative recombination, ultimately shortening the lifetime.[28,29] Various strategies have been employed to mitigate morphological instability, including chemical structure modifications to improve the glass transition

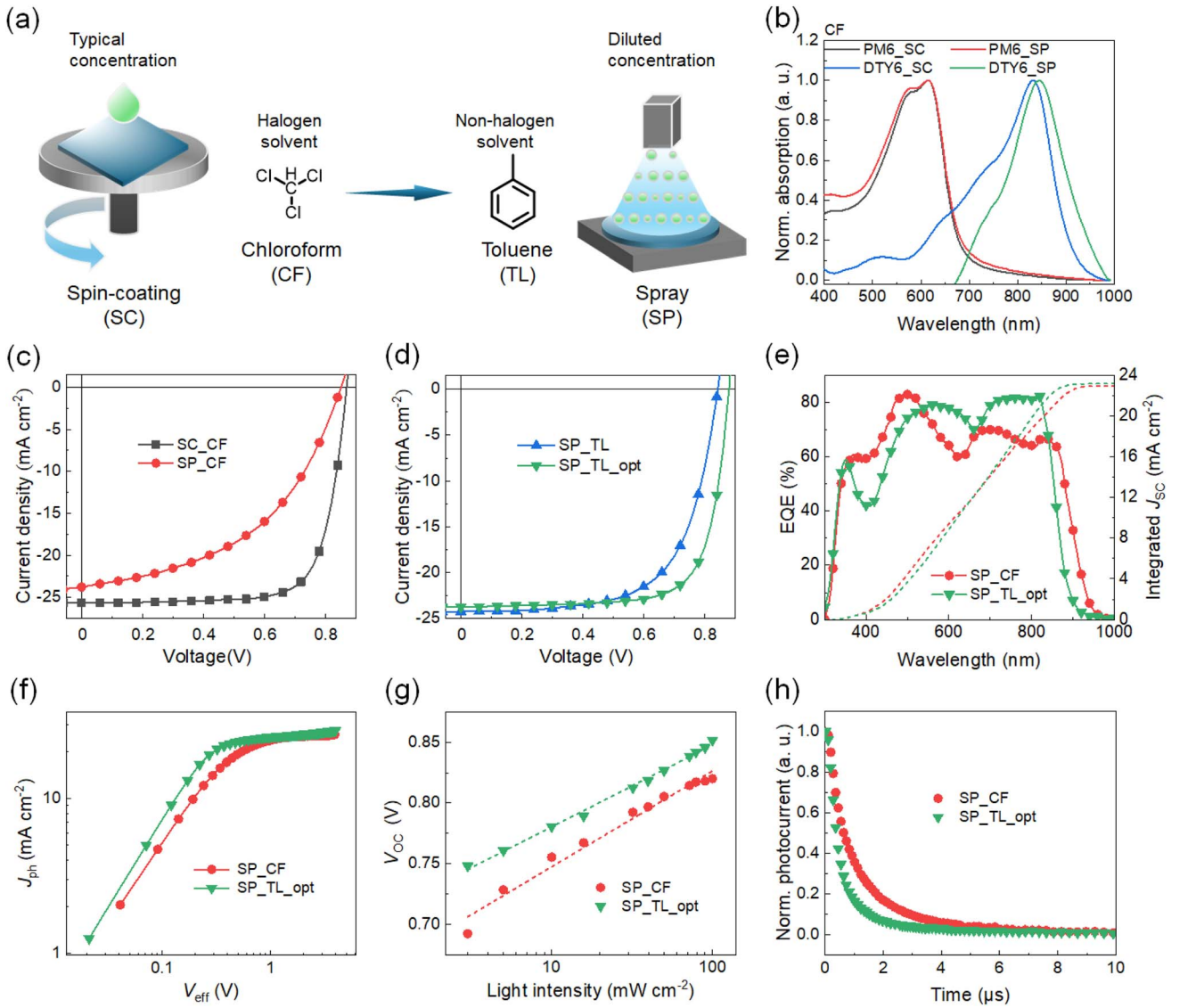

Fig. 1 (a) Chemical structures of solvents employed in this study and schematics of the spin-coating (SC) and spray (SP) techniques; (b) normalized UV-vis absorption spectra of neat PM6 and DTY6 fabricated with the SC or SP techniques in CF solvent. (c) and (d) *J*–*V* characteristics for the OSCs with spin-coating with PM6 : DTY6 with CF solvent (SC_CF), spray coating with PM6 : DTY6 with CF solvent (SP_CF), spray coating with PM6 : DTY6 with TL solvent (SP_TL), and spray coating with PM6 : DTY6:L8BO with TL solvent and further optimization with solvent vapor annealing treatment (SP_TL_opt). (e) EQE curves, (f) J_{ph}–V_{eff} curves, (g) dependence of the open-circuit voltage on light intensity; and (h) transient photocurrent for SP_CF and SP_TL_opt OSCs.

temperature (T_g), construction of alloy-like composites, reduction of the enthalpy change (ΔH) of the BHJ, and dimer/polymerization approaches.[30–39] Extensive research has been conducted to identify the underlying degradation mechanisms, but the insights and analyses from the spin-coating technique cannot be directly transferred to spray coating. Stability investigation of spray-coated devices lags behind, largely because of the limited understanding of film formation kinetics during printing and related morphology stability concerns. Establishing the correlation between morphology and efficiency/stability, along with a comprehensive understanding of film formation kinetics in printed BHJs, is crucial for future advances in sprayed organic photovoltaics.

In this work, spray-coated OSCs were fabricated with an active layer comprising the wide-bandgap polymer donor PM6 and NFA DTY6 under ambient conditions. The devices demonstrate excellent large-area processability and morphological stability with chloroform (CF) and toluene (TL) solvents. The transformation from spin-coating to spray coating results in unexpected PCE and stability losses with processing in CF solvent. TL was selected to tune the morphology of spray-coated PM6 : DTY6 blends, and the optimized TL-sprayed OSCs displayed a PCE of 15.39% under ambient conditions, which is one of the highest efficiencies reported for spray-coated OSCs without an auxiliary method. In addition, the optimized spray-coated OSCs demonstrated excellent long-term morphological stability over 1000 h with negligible losses. The morphological evolution of spray-coated films was systematically investigated with ultraviolet-visible spectroscopy (UV-vis), photoluminescence spectroscopy (PL), atomic force microscopy (AFM) and grazing-incidence wide-angle X-ray scattering (GIWAXS). Combined with charge carrier dynamics analysis, these results illustrate that the rearranged, and more crystalline phase suppresses amorphous clustering and modifies phase separation, thereby optimizing spray-coated films by reducing charge recombination and enhancing charge transport. These findings offer critical insights into overcoming processing-induced limitations and guiding the rational design of high-performance and stable spray-coated OSCs.

2 Results and discussion

2.1 Photovoltaic performances

Schematic diagrams of the spin-coating (SC) and spray-coating (SP) techniques are shown in Fig. 1a. SP without an auxiliary method relies on air pressure to atomize the diluted solution into fine droplets, which are sprayed onto the substrate. These droplets on the substrate merge to form a continuous film, and this differs from the SC method utilizing centrifugal force through high-speed rotation to spread the final films. The chemical structures of PM6 and DTY6 are shown in Fig. S1, SI, and corresponding absorption spectra of neat films fabricated with SC and SP are shown in Fig. 1b. The PM6 exhibits strong absorption at 500–650 nm and DTY6 exhibits strong absorption at 750–900 nm, showing excellent complementary light absorption. Compared to the spin-coated films, the neat PM6 prepared by spray coating shows enhanced A_A transition peaks at 575 nm. The spray-coated DTY6 film exhibits noticeable redshift compared to the spin-coated one, indicating that the film morphology is greatly influenced by different coating techniques. The BHJs fabricated with spin-coating and spray coating are shown in Fig. S2, SI. The DTY6 peak exhibits increased intensity and a redshifted peak location for spray coating, which is consistent with the behavior in neat DT6Y films. To evaluate the effect of solvent on the film formation, OSCs were fabricated with the normal device architecture of ITO/PEDOT : PSS/PM6 : DTY6/PFN-Br/Ag. The active layers of spray-coated OSCs were fabricated in an ambient environment. The current density–voltage (J–V) characteristics of the corresponding devices are shown in Fig. 1c, and the photovoltaic parameters are summarized in Table 1. The spin-coated OSC exhibited a PCE of 16.69%, with an open-circuit voltage (V_{OC}) of 0.872 V, a short-circuit current (J_{SC}) of 25.64 mA cm^{-2}, and a fill factor (FF) of 75.47%, which is consistent with the previous report. For the spray-coated OSCs, the Voc and J_{sc} showed unexpected drops to 0.851 V and 23.78 mA cm^{-2}, respectively. Additionally, the FF clearly dropped to 47.86%, finally giving a poor PCE of 9.62% (denoted as SP_CF). The spin-coated PM6 : DTY6 processed with toluene (TL) exhibits a comparable PCE to that with the CF solvent. TL spray-coated OSCs were fabricated and presented a better PCE of 13.19% than the CF-sprayed OSCs, attributed to the largely increased FF. After systematically optimizing the TL-based ink (Fig. S4–S6, SI), the optimized TL-sprayed OSC exhibited a PCE of 15.39%, along with a V_{OC} of 0.880 V, a J_{SC} of 23.79 mA cm^{-2} and an FF of 73.69% (denoted as SP_TL_opt). The energy losses of the SP_TL and SP_TL_opt devices were calculated as 0.579 and 0.562 eV, respectively. The combination of the advantages of ternary and SVA optimization results in an enhancement of the V_{OC} from 0.846 V to 0.880 V (Fig. S7, SI). The current densities integrated from the EQE spectra are 21.40 and 23.17 mA cm^{-2} for the SP_CF and SP_TL_opt devices, respectively (Fig. 1e), which agree well with the J_{SC} values extracted from the J–V curves.

Table 1 Photovoltaic parameters of OSCs fabricated with the SC and SP techniques

Sample	V_{OC} [V]	J_{SC} [mA cm^{-2}]	$J_{SC,\ EQE}$[a] [mA cm^{-2}]	FF [%]	PCE[b] [%]
SC_CF	0.872	25.64 (25.48 ± 0.12)	25.11	75.47 (74.87 ± 0.38)	16.69 (16.59 ± 0.10)
SP_CF	0.851	23.78 (23.10 ± 0.44)	21.40	47.86 (46.87 ± 1.35)	9.62 (9.13 ± 0.50)
SP_TL	0.846	24.24 (23.77 ± 0.41)	22.92	65.20 (64.28 ± 0.57)	13.19 (12.90 ± 0.17)
SP_TL_opt	0.880	23.79 (23.65 ± 0.18)	23.17	73.69 (73.11 ± 0.61)	15.39 (15.20 ± 0.14)

[a] Values in parentheses are the current densities integrated from the EQE spectra. [b] Average values were obtained from 10 separate devices.

The charge generation, extraction and recombination characteristics were evaluated in the SP_CF and SP_TL_opt devices. Fig. 1f presents the photocurrent density (J_{ph}) *versus* the effective voltage (V_{eff}) of the devices. Compared to the exciton dissociation probability (P_{diss}) of 83.6% for the SP_CF device, the higher P_{diss} of 90.4% for the SP_TL_opt device indicates the higher exciton dissociation and charge collection efficiency. Meanwhile, the semilogarithmic plot of V_{OC} as a function of the light intensity exhibits a linear relationship with a slope of kT/q. A stronger dependence of V_{oc} on the light intensity with a larger slope of kT/q will be observed if Shockley–Read–Hall (SRH) recombination is involved. As depicted in Fig. 1g, the fitted slopes are 1.34 and 1.14 kT/q, indicating the lower SRH recombination of the SP_TL_opt device than that of SP_CF device. Transient photocurrent measurements were conducted to probe the competition between charge carrier extraction and recombination (Fig. 1h). The SP_TL_opt device exhibited a shorter charge extraction time (τ_{TPC}) of 0.48 μs than the SP_CF (0.97 μs). These findings are consistent with the observed enhanced FF of the optimized device.

2.2 Drying kinetics

To gain deeper insight into the conformation and aggregation kinetics of blends, *in situ* UV-vis measurements were performed under ambient conditions (Fig. S8, SI). For spin-coated films, fast film formation within 1s was observed (Fig. 2a), and the interaction of the active components occurred. To understand the effect of solvents and processing techniques on film morphology, the temporal evolution of the absorption peaks and intensities for the polymer and NFAs was determined (Fig. 2b and c). Four film formation stages are defined as solvent evaporation, planarization of the polymer, interaction with a solution of the acceptor, and a final stable stage, corresponding to the different signal evolution trends observed for the donor and acceptor materials (II and III) in the spin-coating. Such stages in spin-coating processes suggest a stepwise, favorable planarization of the H-aggregated phase. As shown in Fig. 2d and g, spray-coated films exhibited totally different film formation, and both SP_CF and SP_TL films showed enhanced intensity along with formation time without a very noticeable red/blue wavelength shift compared to the spin-coated

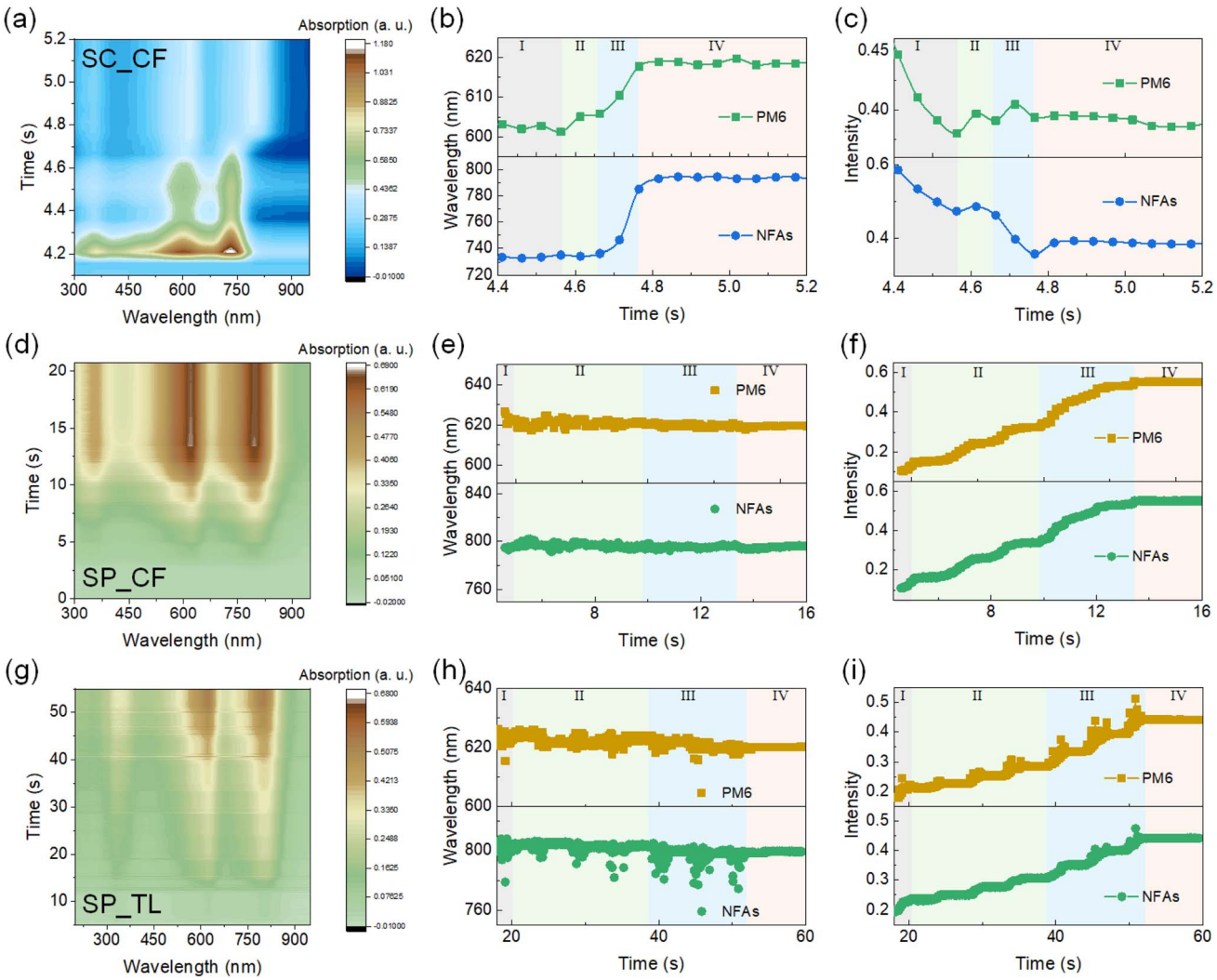

Fig. 2 (a–c) *In situ* UV-vis 2D mapping of the film formation kinetics for SC_CF, SP_CF and SP_TL, respectively. (d–f) Primary peak positions and (g–i) the corresponding normalized peak intensities of SC_CF, SP_CF and SP_TL during the *in situ* experiment.

films (Fig. 2e, f, h and i). The film formation by spray coating can also be divided into four stages. The initial stage I, corresponding to the deposition of spray droplets onto the substrate, and the stable stage IV exhibited clear stage characteristics. We define the distinction between stage II and III as the rate of intensity increases, which correlates with the film formation of the CF and TL solvents. In stage I, the intensity for the CF spray-coated film increased to 0.05, whereas that for TL increased to 0.03. The absorption intensity gradually increases for both PM6 and NFAs. This stage denotes sprayed droplets deposited on the substrate and initial film formation. After entering stage II, a noticeable platform and subsequent upward trend occur at certain time periods (about 1 s for CF and 4 s for TL). The absorption intensity increase for CF is calculated to be about 0.09 for one step, greater than that for TL (0.01). The smoother curve of PM6 and NFAs without significant plateaus or sudden jumps suggests that the crystallization kinetics for SP_TL are relatively mild. As TL evaporates more slowly than CF, the photo-active materials likely undergo a longer period of phase formation and reorganization, which may affect the final film morphology and photovoltaic performance.[40,41] In stage III, note that the peak wavelength of the NFAs exhibited discretization in the TL solvent, whereas it is stable in CF. Some discretization was also observed in stage II in TL. The intensity for the CF spray-coated film jumped clearly from 0.32 to 0.52 and established new plateaus. A similar phenomenon was also observed in the TL-processed film. The intensity growth is lower than that with CF, but also exhibited an increase of 2.5 times compared to stage II for both PM6 and NFAs. Here, we define stage III as the accumulation growth phase. Both stage I and stage II exhibit plateau regions and intensity enhancement regions. However, the spray process continuously deposits solvent onto the substrate, preventing complete solvent evaporation and film formation. Instead, the system remains in an intermediate state between film formation and continued liquefaction. In stage III, as the spray process is concluded, the incomplete film formation from the earlier stages and the imminent termination of spray coating lead to a significant intensity increase. This corresponds to the crucial assembly and aggregation states of the polymer donor and NFAs. The CF process results in film formation in a single step, whereas the TL process exhibits three distinct stages. This can be attributed to the slower evaporation rate of toluene, which provides donor and acceptor materials with additional time to assemble within the solvent environment. This extended assembly period likely promotes a more uniform phase separation and an optimized blend network. In the final stage, nearly all the solvent has fully evaporated. The absence of further changes in peak positions and peak intensities indicates that no additional transitions or aggregation occur among the materials. The delayed film formation in SP_TL may prevent premature phase separation, facilitating the formation of a more interconnected donor–acceptor network, which is consistent with the enhanced FF in OSCs.

2.3 Film morphology

The surface morphology of the active layers was characterized by atomic force microscopy (AFM) (Fig. 3a and Fig. S9, SI). The SC_CF film exhibited smooth surfaces with a roughness of 1.27 nm and relatively little phase separation. In contrast, the SP_CF film shows significantly rougher surfaces (RMS = 14.7 nm) and granular aggregation. Comparable uniform surfaces are observed in all SP_TL films, corresponding to enhanced FF. Note that the SP_TL_opt film exhibited a clearly fibrous network, reported to enable multi-scale structure that enhances carrier extraction and transportation.[42]

To gain deeper insights into the molecular packing and orientation of the crystallinity of the active layers, grazing-incidence wide-angle X-ray scattering (GIWAXS) measurements were conducted. Fig. 3b shows the 2D GIWAXS images of the samples. Fig. 3c shows the OOP and IP cuts of the samples. All the samples show a (010) peak ~1.7 $Å^{-1}$ along the OOP direction and a (100) peak ~0.3 $Å^{-1}$ in all directions, suggesting a face-on crystalline structure in the active layer. All the peak details are summarized in Tables S7 and S8, SI. The SC_CF active layer exhibits a higher intensity than the sprayed active layer at the (010) peak along the OOP direction. Moreover, the SC_CF sample shows a higher intensity distribution in the range of 45–90° for the tube cut of the (100) peak, suggesting more face-on orientation crystallinity structure. It has been found that the CF host solvent is not favorable for the active layer to form a structure with face-on crystallinity with the spray technique. For the spray-coated active layers with the toluene solvent, we noted that the crystallinity intensity is lower for both crystallinity peaks, and the (010) peak position (1.68 $Å^{-1}$) is higher than that for the sprayed CF active layer (1.65 $Å^{-1}$), suggesting more compact π–π stacking crystallinity. With the solvent vaper annealing (SVA) post-treatment, the π–π stacking crystallinity of the toluene-sprayed active layer is further compacted and enhanced, showing increased peak intensity and a larger peak position (1.71 $Å^{-1}$). In addition, the slightly increased distribution in the 45–90° range of the (100) peak in the tube cut suggests an enhanced face-on orientation of the crystallinity structure. We also noted that there are peaks appearing at 0.48 $Å^{-1}$ and 1.46 $Å^{-1}$, suggesting that with the SVA post-treatment, the side chains are rearranged, and a higher level of crystallinity is generated, favoring charge carrier transportation. The appearance of side peaks indicates that more crystalline phases are formed inside the film.

Optical spectroscopy was used to analyze the film morphology according to a previous report.[43,44] Based on the deconvolution data (Fig. S10, and Tables S4, S5, SI), the relative energy transfer quantum yields of all films were calculated from the amorphous to the ordered phase and plotted in Fig. 3e. $Ø_{RET}/Ø_{PL}$ was calculated to be 0.35 in the CF_SP film, higher than 0.28 in the TL_SP film. Combined with much phase separation and crystallinity in the CF_SP film, this indicated that the CF_SP film has a dispersive amorphous phase, and FF loss mainly comes from exciton recombination, in contrast to the TL counterparts. The $Ø_{RET}/Ø_{PL}$ of the optimized TL devices reached 0.45, exhibiting a more efficient relative energy transfer quantum yield.[39,45] To better understand the film formation changes in detail, time-resolved photoluminescence (TRPL) spectra for the SP_CF and SP_TL_opt blends at various wavelengths from 950–1500 nm were recorded using an 810 nm laser

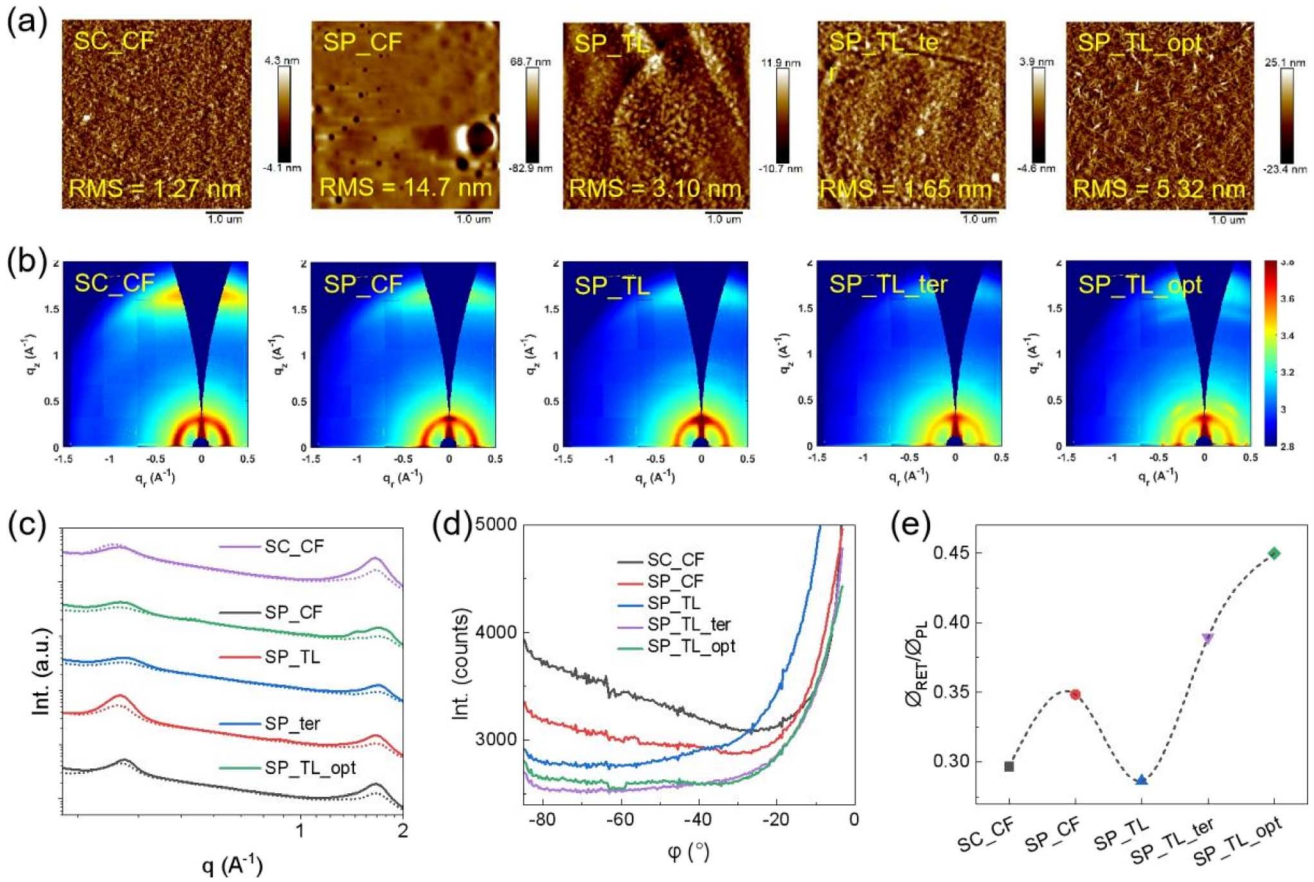

Fig. 3 (a) AFM height images and (b) 2D GIWAXS images of the representative active layers. (c) 1D scattering profiles of out-of-plane (OOP, solid line) and in-plane (IP, dashed line) cuts and (d) tube cuts for the azimuthal (100) peak corresponding to the active layers. (e) Relative energy transfer quantum yield from the amorphous to the ordered phase for all films.

to excite the films (Fig. S11, SI). The extracted lifetimes (τ_1, τ_2, τ_3) are summarized in Table S6 (SI). Compared to the SP_CF film, the SP_TL_opt film exhibits shorter PL lifetimes, indicating more efficient exciton dissociation and charge transportation in the SP_TL_opt films. The enhancement may benefit from fiber-like charge transport pathways with suppressed likelihood of charge recombination.

2.4 Thermal stability

To investigate the long-term stability of the SP_CF and SP_TL_opt films, thermal stability measurements were performed on inverted OSCs with the structure ITO/ZnO/active layer/MoO_X/Ag, which has been proved to be valid to evaluate the stability of active layers as stable buffers. The thermal stability was evaluated at a temperature of 65 °C (Fig. 4a) in a nitrogen-filled glovebox on a hot plate. The normalized photovoltaic parameters are plotted with respect to the thermal ageing time. The V_{OC} dropped to 36%, J_{SC} to 66%, and FF to 65% in the SP_CF device. However, there was almost no significant fluctuation for the SP_TL_opt devices after thermal annealing, indicating robust stability for this blend. The SP_TL_opt device retained the highest 97% of its original PCE after being thermally annealed for about 1000 h, indicating excellent thermal stability. Due to the low diffusion coefficient, the NFA-based OSCs exhibited a predominant loss of FF compared to fullerene-based systems. Hence, to further verify the V_{OC} and J_{SC} losses in the SP_CF devices, we conducted long-term stability tests with a PEDOT-F interface, where PEDOT-F was utilized to modify charge extraction for superior stability. A similar trend was also observed in the PEDOT-F hole-transporting layer. The light stability of these OSCs was also investigated under one-sun illumination. As demonstrated in Fig. 4c and d, the SP_TL_opt exhibited better photostability, retaining 93% and 94% of the original PCE after 180 h of illumination in MoO_x and PEDOT-F as buffer layers, respectively.

To investigate the degeneration of active layers, the surface morphology of the aged active layers is evaluated with AFM (Fig. S12, SI). The SP_CF film shows rougher (RMS = 14.7 nm) and enlarged granular aggregation. A comparable uniform film was observed in the SP_TL_opt film (4.33 nm), which corresponds to stable performance. From the GIWAXS data (Fig. S13, SI), the SP_CF film exhibits an intensity increase and constant positions both for (100) and (010) peaks after the degradation. In addition, the (100) peak intensity among the whole angle range increased, especially for −90° to −45°, suggesting growth of crystallinity, especially for the face-on orientation. For the SP_TL_opt film, although the peaks at 0.48 $Å^{-1}$ and 1.46 $Å^{-1}$ are

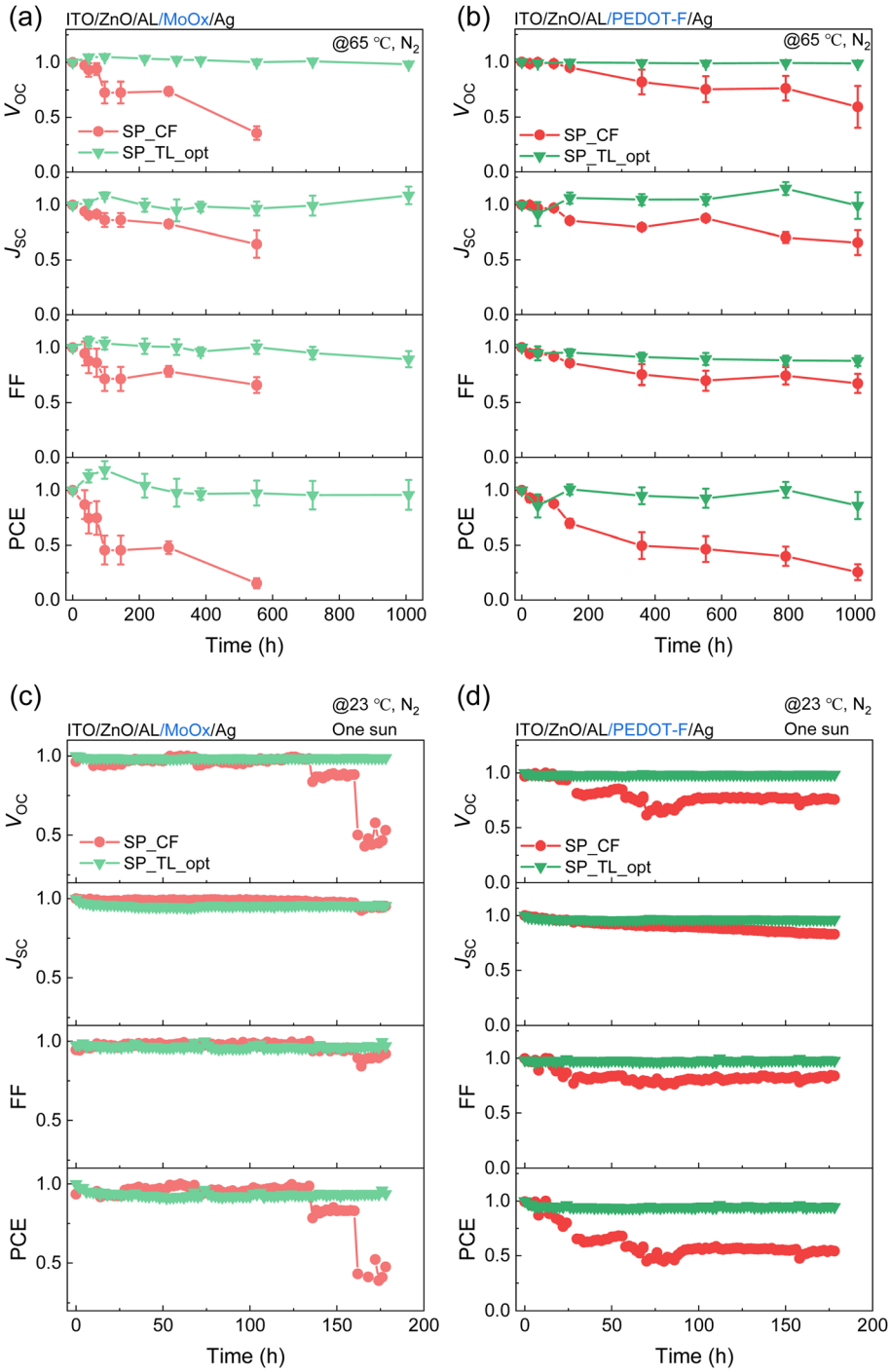

Fig. 4 The thermal and photostability of SP_CF and SP_TL_opt devices fabricated with two different device architectures: ITO/ZnO/active layer/MoO_x/Ag and ITO/ZnO/active layer/PEDOT-F/Ag. (a and b) Thermal stability was evaluated under continuous thermal aging at 65 °C under a dry nitrogen atmosphere without encapsulation. (c and d) Photostability was assessed under continuous one-sun illumination at 23 °C under a dry nitrogen atmosphere without encapsulation.

associated with the loss of side chain crystallinity, the (100) and (010) peaks show no significant changes after the degradation study. This suggests that the main crystallinity framework remains almost constant, which could explain the outstanding stability for the corresponding OSCs. The drying dynamics of SP_CF are very fast, but this leads to unstable crystallization, making the structure easily degraded during ageing. In contrast, the SP_TL_opt film allows more time for crystal formation and stabilization, so even after 500 h, the main crystalline framework remains intact, corresponding to stable performance. Optical spectroscopy was also used to analyze the film morphology. The SP_CF film shows $Ø_{RET}/Ø_{PL}$ decreased to

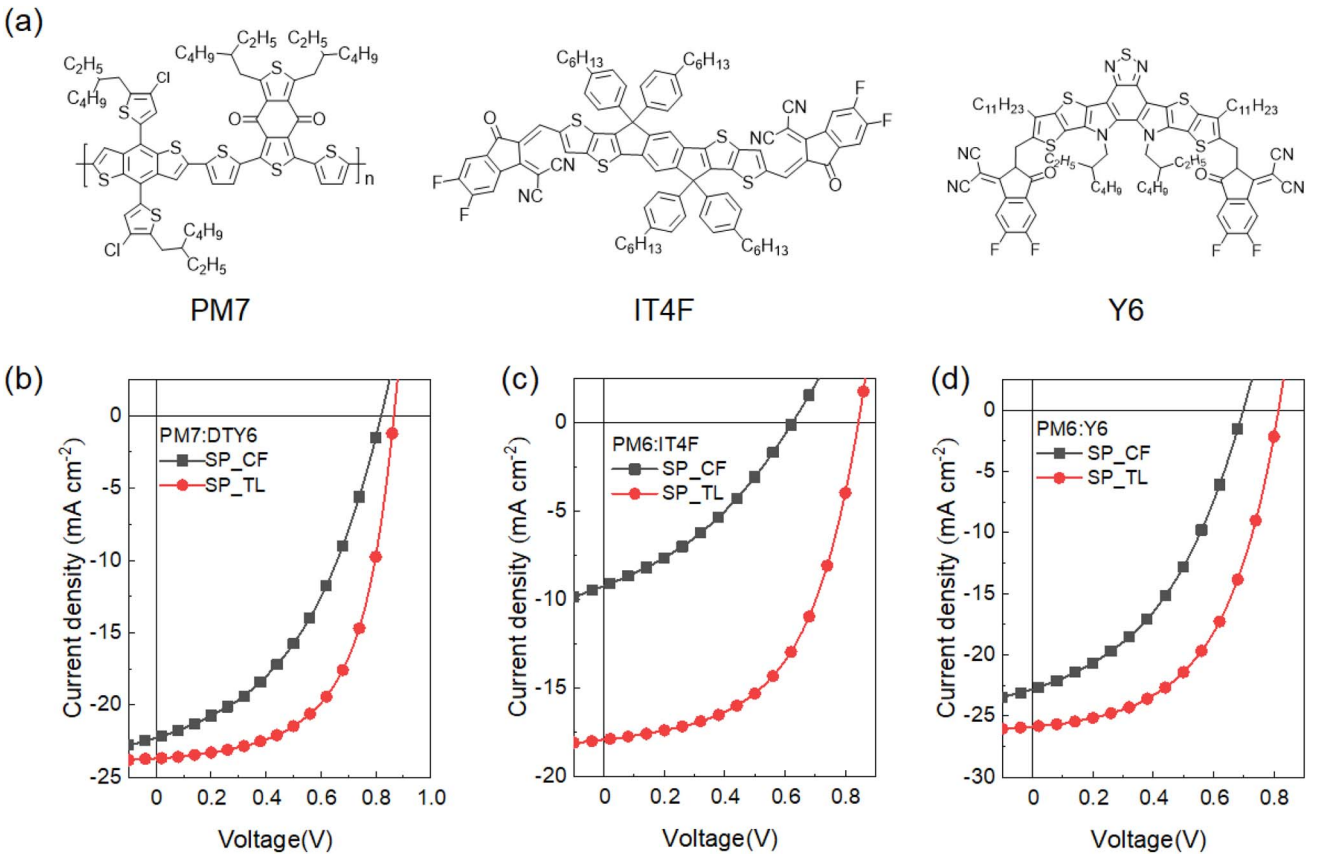

Fig. 5 (a) Chemical structures of PM7, IT4F and Y6 employed in this study. (b–d) *J*–*V* characteristics for the OSCs with spray coating with PM7 : DTY6, PM6 : IT4F and PM6 : Y6 with CF and TL solvent.

0.33, indicating the formation of amorphous clusters in the NFAs, whereas $Ø_{RET}/Ø_{PL}$ remained stable in SP_TL_opt.

As the morphology of the sprayed OSCs can be finely adjusted, the universality of the spray-coating technique was confirmed with devices based on another polymer donor, PM7 and two acceptors, IT4F and Y6 (Fig. 5 and Table S13, SI). Compared with the SP_CF based devices, using the TL solvent showed improvements in all three key parameters. These results are consistent with those for PM6 : DTY6-based devices and reinforce the universality of the spray-coating technique.

3 Conclusion

In summary, we finely tuned the morphology of spray-coated OSCs during the transformation from a spin-coating to spray-coating technique, using a non-halogenated solvent, ternary component and solvent vapor annealing treatment. The optimized spray-coated devices achieved a record PCE of 15.39%, driven by simultaneous improvements in modified FF and V_{OC}. *In situ* UV-vis measurements provided insights into the film formation kinetics related to the conformation and aggregation in the BHJ. AFM, GIWAXS and optical analyses revealed that the SP_TL_opt film developed a fibrous structure, improved the molecular arrangement, and exhibited a less amorphous morphology compared to SP_CF. Moreover, the morphology investigation of the aged films also illustrated that more crystalline phases are formed inside the SP_TL_opt films, resulting in a more robust morphology. Carrier characteristics showed that the PCE improvement was primarily due to the reduced charge recombination and modified extraction. These findings provide valuable guidance for controlling thin-film morphology to simultaneously optimize the performance and stability of spray-coated organic photovoltaic devices.

Conflicts of interest

The authors declare no competing interests.

Data availability

All data generated or analyzed during this study are included in this published article and its SI.

Acknowledgements

Q. W., K. A., X. C., and X. J. contributed equally to this work. This work was financially supported by the National Key Research and Development Program of China (2022YFB4200400), the National Natural Science Foundation of China (52394273 and 52373179), the TCL Science and Technology Innovation Fund (20242065), and the Fund of

Guangdong Provincial Key Laboratory of Luminescence from Molecular Aggregates (2023B1212060003). X. Jiang and S.V. Roth acknowledge funding by the Federal Institute for Research on Building, Urban Affairs and Spatial Development on behalf of the Federal Ministry of the Interior, Building and Community with funds from the Zukunft Bau research programme under grant "Nachhaltige Sonnenschutzsysteme aus hochfester Zellulose zur Umwandlung von Sonnenenergie".

References

1 H. Yang, C. Cui and Y. Li, Effects of heteroatom substitution on the photovoltaic performance of donor materials in organic solar cells, *Acc. Mater. Res.*, 2021, **2**(11), 986–997, DOI: **10.1021/accountsmr.1c00119**.

2 X. Wang, H. Chen, J. Yuan, *et al.*, Precise fluorination of polymeric donors towards efficient non-fullerene organic solar cells with balanced open circuit voltage, short circuit current and fill factor, *J. Mater. Chem. A*, 2021, **9**(26), 14752–14757, DOI: **10.1039/D1TA01500A**.

3 Y. Xu, Y. Cui, H. Yao, *et al.*, A new conjugated polymer that enables the integration of photovoltaic and light-emitting functions in one device, *Adv. Mater.*, 2021, **33**(22), 2101090, DOI: **10.1002/adma.202101090**.

4 J. Qin, C. An, J. Zhang, *et al.*, 15.3% efficiency all-small-molecule organic solar cells enabled by symmetric phenyl substitution, *Sci. China Mater.*, 2020, **63**(7), 1142–1150, DOI: **10.1007/s40843-020-1269-9**.

5 Y. Cui, Y. Xu, H. Yao, *et al.*, Single-junction organic photovoltaic cell with 19% efficiency, *Adv. Mater.*, 2021, **33**(41), 2102420, DOI: **10.1002/adma.202102420**.

6 Q. Liu, J. Fang, J. Wu, *et al.*, Tuning aggregation behavior of polymer donor via molecular-weight control for achieving 17.1% efficiency inverted polymer solar cells, *Chin. J. Chem.*, 2021, **39**(7), 1941–1947, DOI: **10.1002/cjoc.202100112**.

7 R. Ma, X. Jiang, J. Fu, *et al.*, Revealing the underlying solvent effect on film morphology in high-efficiency organic solar cells through combined ex situ and in situ observations, *Energy Environ. Sci.*, 2023, **16**(5), 2316–2326, DOI: **10.1039/D3EE00294B**.

8 J. Fu, P. W. K. Fong, H. Liu, *et al.*, 19.31% binary organic solar cell and low non-radiative recombination enabled by non-monotonic intermediate state transition, *Nat. Commun.*, 2023, **14**(1), 1760, DOI: **10.1038/s41467-023-37526-5**.

9 S. Qu, J. Yu, J. Cao, *et al.*, Highly efficient organic solar cells enabled by a porous ZnO/PEIE electron transport layer with enhanced light trapping, *Sci. China Mater.*, 2020, **64**, 808–819, DOI: **10.1007/s40843-020-1508-7**.

10 D. Li, N. Deng, Y. Fu, *et al.*, Fibrillization of non-fullerene acceptors enables 19% efficiency pseudo-bulk heterojunction organic solar cells, *Adv. Mater.*, 2023, **35**(6), 2208211, DOI: **10.1002/adma.202208211**.

11 S. Dong, T. Jia, K. Zhang, *et al.*, Single-component non-halogen solvent-processed high-performance organic solar cell module with efficiency over 14%, *Joule*, 2020, **4**(9), 2004–2016, DOI: **10.1016/j.joule.2020.07.028**.

12 Y. Cui, H. Yao, J. Zhang, *et al.*, Single-junction organic photovoltaic cells with approaching 18% efficiency, *Adv. Mater.*, 2020, **32**(19), 1908205, DOI: **10.1002/adma.201908205**.

13 C. Li, J. Zhou, J. Song, *et al.*, Non-fullerene acceptors with branched side chains and improved molecular packing to exceed 18% efficiency in organic solar cells, *Nat. Energy*, 2021, **6**(6), 605–613, DOI: **10.1038/s41560-021-00820-x**.

14 Z. Li, X. Li, J. Xue, *et al.*, A-DA′ DA type acceptor with a benzoselenadiazole A′-Unit enables efficient organic solar cells, *ACS Energy Lett.*, 2023, **8**(6), 2488–2495, DOI: **10.1021/acsenergylett.3c00743**.

15 Y. Chen, F. Bai, Z. Peng, *et al.*, Asymmetric alkoxy and alkyl substitution on nonfullerene acceptors enabling high-performance organic solar cells, *Adv. Energy Mater.*, 2021, **11**(3), 2003141, DOI: **10.1002/aenm.202003141**.

16 Y. Jiang, F. Liu and X. Zhu, Single-junction organic solar cells with a power conversion efficiency of more than 20%, *Nat. Energy*, 2024, **9**(8), 930–931, DOI: **10.1038/s41560-024-01558-y**.

17 H. Chen, Y. Huang, R. Zhang, *et al.*, Organic solar cells with 20.82% efficiency and high tolerance of active layer thickness through crystallization sequence manipulation, *Nat. Mater.*, 2025, 1–10, DOI: **10.1038/s41563-024-02062-0**.

18 C. Chen, L. Wang, W. Xia, *et al.*, Molecular interaction induced dual fibrils towards organic solar cells with certified efficiency over 20%, *Nat. Commun.*, 2024, **15**(1), 6865, DOI: **10.1038/s41467-024-51359-w**.

19 Y. Jiang, S. Sun, R. Xu, *et al.*, Non-fullerene acceptor with asymmetric structure and phenyl-substituted alkyl side chain for 20.2% efficiency organic solar cells, *Nat. Energy*, 2024, **9**(8), 975–986, DOI: **10.1038/s41560-024-01557-z**.

20 L. Zhu, M. Zhang, G. Zhou, *et al.*, Achieving 20.8% organic solar cells via additive-assisted layer-by-layer fabrication with bulk pin structure and improved optical management, *Joule*, 2024, **8**(11), 3153–3168, DOI: **10.1016/j.joule.2024.08.001**.

21 L. Wang, C. Chen, Z. Gan, *et al.*, Diluted Ternary Heterojunctions to Suppress Charge Recombination for Organic Solar Cells with 21% Efficiency, *Adv. Mater.*, 2025, **37**(13), 2419923, DOI: **10.1002/adma.202419923**.

22 K. Chang, Y. Li, H. Xia, *et al.*, Organic Photovoltaics Printed via Sheet Electrospray Enabled by Quadrupole Electrodes, *ACS Appl. Mater. Interfaces*, 2021, **13**(47), 56375–56384, DOI: **10.1021/acsami.1c14104**.

23 E. L. K. Spooner, E. J. Cassella, J. A. Smith, *et al.*, Air-knife-assisted spray coating of organic solar cells, *ACS Appl. Mater. Interfaces*, 2023, **15**(33), 39625–39635, DOI: **10.1021/acsami.3c05306**.

24 A. Liu, W. Zheng, X. Yin, *et al.*, Manipulate micrometer surface and nanometer bulk phase separation structures in the active layer of organic solar cells via synergy of ultrasonic and high-pressure gas spraying, *ACS Appl. Mater. Interfaces*, 2019, **11**(11), 10777–10784, DOI: **10.1021/acsami.8b22215**.

25 K. Chang, Y. Li, G. Du, *et al.*, Efficient non-fullerene organic photovoltaics printed by electrospray via solvent

engineering, *ACS Appl. Mater. Interfaces*, 2020, **12**(24), 27405–27415, DOI: 10.1021/acsami.0c03632.

26 K. Chang, B. Yu, L. Liu, *et al.*, Efficient Fully-Sprayed Organic Solar Cells with Coffee-Ring-Free Photoactive Layer and Alloy Top-Electrode, *Adv. Mater. Technol.*, 2023, **8**(11), 2201921, DOI: 10.1002/admt.202201921.

27 H. Zhao, L. Wang, Y. Wang, *et al.*, Solvent-Vapor-Annealing-Induced Interfacial Self-Assembly for Simplified One-Step Spraying Organic Solar Cells, *ACS Appl. Energy Mater.*, 2021, **4**(7), 7316–7326, DOI: 10.1021/acsaem.1c01446.

28 H. Xu, J. Han, A. Sharma, *et al.*, Progress in the Stability of Small Molecule Acceptor-Based Organic Solar Cells, *Adv. Mater.*, 2025, **37**(4), 2407119, DOI: 10.1002/adma.202407119.

29 S. Yoon, E. Y. Shin, N. K. Cho, *et al.*, Progress in morphology control from fullerene to nonfullerene acceptors for scalable high-performance organic photovoltaics, *J. Mater. Chem. A*, 2021, **9**(44), 24729–24758, DOI: 10.1039/D1TA06861J.

30 B. Fan, W. Gao, X. Wu, *et al.*, Importance of structural hindrance in performance–stability equilibrium of organic photovoltaics, *Nat. Commun.*, 2022, **13**(1), 5946, DOI: 10.1038/s41467-022-33754-3.

31 B. Fan, W. Gao, R. Zhang, *et al.*, Correlation of local isomerization induced lateral and terminal torsions with performance and stability of organic photovoltaics, *J. Am. Chem. Soc.*, 2023, **145**(10), 5909–5919, DOI: 10.1021/jacs.2c13247.

32 D. L. Ma, Q. Q. Zhang and C. Z. Li, Unsymmetrically Chlorinated Non-Fused Electron Acceptor Leads to High-Efficiency and Stable Organic Solar Cells, *Angew. Chem., Int. Ed.*, 2023, **62**(5), e202214931, DOI: 10.1002/anie.202214931.

33 H. Wang, C. Cao, H. Chen, *et al.*, Oligomeric acceptor: A "two-in-one" strategy to bridge small molecules and polymers for stable solar devices, *Angew. Chem.*, 2022, **134**(23), e202201844, DOI: 10.1002/anie.202201844.

34 L. Zhang, Z. Zhang, D. Deng, *et al.*, "N-π-N" Type Oligomeric Acceptor Achieves an OPV Efficiency of 18.19% with Low Energy Loss and Excellent Stability, *Advanced Science*, 2022, **9**(23), 2202513, DOI: 10.1002/advs.202202513.

35 J. W. Lee, C. Sun, T. N. L. Phan, *et al.*, Trimerized small-molecule acceptors enable high-performance organic solar cells with high open-circuit voltage and prolonged lifetime, *Energy Environ. Sci.*, 2023, **16**(8), 3339–3349, DOI: 10.1039/D3EE00272A.

36 W. Song, K. Yu, J. Ge, *et al.*, Entangled structure morphology by polymer guest enabling mechanically robust organic solar cells with efficiencies of over 16.5, *Matter*, 2022, **5**(6), 1877–1889, DOI: 10.1016/j.matt.2022.03.012.

37 R. Sun, T. Wang, Q. Fan, *et al.*, 18.2%-efficient ternary all-polymer organic solar cells with improved stability enabled by a chlorinated guest polymer acceptor, *Joule*, 2023, **7**(1), 221–237, DOI: 10.1016/j.joule.2022.12.007.

38 R. Sun, Y. Wu, X. Yang, *et al.*, Single-junction organic solar cells with 19.17% efficiency enabled by introducing one asymmetric guest acceptor, *Adv. Mater.*, 2022, **34**(26), 2110147, DOI: 10.1002/adma.202110147.

39 K. An, W. Zhong, F. Peng, *et al.*, Mastering morphology of non-fullerene acceptors towards long-term stable organic solar cells, *Nat. Commun.*, 2023, **14**(1), 2688, DOI: 10.1038/s41467-023-38306-x.

40 H. Zhang, Y. Liu, G. Ran, *et al.*, Sequentially Processed Bulk-Heterojunction-Buried Structure for Efficient Organic Solar Cells with 500 nm Thickness, *Adv. Mater.*, 2024, **36**(25), 2400521, DOI: 10.1002/adma.202400521.

41 L. Zhu, M. Zhang, G. Zhou, *et al.*, Efficient Organic Solar Cell with 16.88% Efficiency Enabled by Refined Acceptor Crystallization and Morphology with Improved Charge Transfer and Transport Properties, *Adv. Energy Mater.*, 2020, **10**(18), 1904234, DOI: 10.1002/aenm.201904234.

42 L. Zhu, M. Zhang, J. Xu, *et al.*, Single-junction organic solar cells with over 19% efficiency enabled by a refined double-fibril network morphology, *Nat. Mater.*, 2022, **21**(6), 656–663, DOI: 10.1038/s41563-022-01244-y.

43 R. Wang, L. Lüer, S. Langner, *et al.*, Understanding the microstructure formation of polymer films by spontaneous solution spreading coating with a high-throughput engineering platform, *ChemSusChem*, 2021, **14**(17), 3590–3598, DOI: 10.1002/cssc.202100927.

44 J. Zhang, L. Zhang, X. Wang, *et al.*, Reducing photovoltaic property loss of organic solar cells in blade-coating by optimizing micro-nanomorphology via nonhalogenated solvent, *Adv. Energy Mater.*, 2022, **12**(14), 2200165, DOI: 10.1002/aenm.202200165.

45 B. Zou, W. Wu, T. A. Dela Peña, *et al.*, Step-by-step modulation of crystalline features and exciton kinetics for 19.2% efficiency ortho-xylene processed organic solar cells, *Nano-Micro Lett.*, 2024, **16**(1), 30, DOI: 10.1007/s40820-023-01241-z.